Available online at www.sciencedirect.com
ScienceDirect
Journal of Power Sources 162 (2006) 356–368
JOURNAL OF POWER SOURCES
www.elsevier.com/locate/jpowsour

Transient operation and shape optimization of a single PEM fuel cell

Sheng Chen [a], Juan C. Ordonez [a,*], Jose V.C. Vargas [b], Jose E.F. Gardolinski [b], Maria A.B. Gomes [c]

[a] *Department of Mechanical Engineering, Center for Advanced Power Systems, and Sustainable Energy Science and Engineering Center, Florida State University, Tallahassee, FL 32310, USA*
[b] *Department of Mechanical Engineering, Federal University of Paraná, C.P. 19011, Curitiba, Paraná 81531-990, Brazil*
[c] *Department of Chemistry, Federal University of Paraná, C.P. 19011, Curitiba, Paraná 81531-990, Brazil*

Received 2 May 2006; received in revised form 30 June 2006; accepted 30 June 2006
Available online 17 August 2006

Abstract

Geometric design, including the internal structure and external shape, considerably affect the thermal, fluid, and electrochemical characteristics of a polymer electrolyte membrane (PEM) fuel cell, which determine the polarization curves as well as the thermal and power inertias. Shape optimization is a natural alternative to improve the fuel cell performance and make fuel cells more attractive for power generation. This paper investigates the internal and external structure effects on the fuel cell steady and transient operation with consideration of stoichiometric ratios, pumping power, and working temperature limits. The maximal steady state net power output and the fuel cell start-up time under a step-changed current load characterize the fuel cell steady and transient performance respectively. The one-dimensional PEM fuel cell (PEMFC) thermal model introduced in a previous work [J.V.C. Vargas, J.C. Ordonez, A. Bejan, Constructal flow structure for a PEM fuel cell, Int. J. Heat Mass Transfer 47 (2004) 4177–4193] is amended to simulate the fuel cell transient start-up process. The shape optimization consists of the internal and external PEMFC structure optimization. The internal optimization focuses on the optimal allocation of fuel cell compartment thicknesses. The external optimization process seeks the PEM fuel cell optimal external aspect ratios. These two levels of optimizations pursue the optimal geometric design with quick response to the step loads and large power densities. Appropriate dimensionless groups are identified and the numerical results are presented in dimensionless charts for general engineering design. The universality of the general optimal shape found is also discussed.

Keywords: PEMFC design; Constructal design; Thermal inertia

1. Introduction

Fuel cells are expected to become of common use in stationary power generation and transportation systems [1–3]. The energy industry is searching for alternative power generation modes in order to reduce its dependency on conventional fossil fuel and, in parallel, for means to improve systems and processes efficiencies. Fuel cell technology also benefits the environment by cutting down a large amount of green house gas (CO_2) and other poisonous exhausts (NO_x, SO_x), through the introduction of the fuel cells into transportation and power generation systems. Furthermore, submarines and aircrafts with fuel cell power supply system could dramatically decrease cruising noise to comply with military requirements. PEMFC is also widely investigated because of its high efficiency and the potential for utilization in vehicular and portable applications. Fuel cell technology has been improving in several aspects such as materials, thermodynamic management and flow structure. In this paper, we focus on the flow structure optimization, which has the potential to improve the fuel cell performance, involving steady state and transient operation.

The flow structure optima are the results of numerical simulation of mathematical models that express the physics of fuel cell operations. Kumar and Reddy [4] present a mathematic model applying Navier–Stokes equations to predict the effects of shape and size of flow channel on the fuel cell performance. Yi and Nguyen [5] developed a two-dimensional cathode model to investigate the performance of interdigitated fuel cells. Zhou and Liu [6] presented a three-dimensional steady state model for PEM fuel cells, Hu et al. [7,8] introduced a three-dimensional

* Corresponding author. Tel.: +1 850 6448405; fax: +1 850 6447456.
E-mail address: ordonez@caps.fsu.edu (J.C. Ordonez).

0378-7753/$ – see front matter © 2006 Elsevier B.V. All rights reserved.
doi:10.1016/j.jpowsour.2006.06.088

Nomenclature

Δa	variation of quantity a between two conditions
A	area (m^2)
$\tilde{A}$	dimensionless area
A_s	fuel cell cross-sectional area (m^2)
A_w	the wall area (m^2)
A_{wet}	the wetted surface area (m^2)
B	dimensionless constant in Eq. (14)
c_p	specific heat at constant pressure ($kJ\,kg^{-1}\,K^{-1}$)
c_v	specific heat at constant volume ($kJ\,kg^{-1}\,K^{-1}$)
CV	control volume
D	Knudsen diffusion coefficient ($m^2\,s^{-1}$)
D_h	gas channel hydraulic diameter (m)
$\dot{E}$	energy flow rate (W)
$\tilde{E}$	dimensionless energy flow rate
f	friction factor
F	faraday constant (96,500 C equiv.$^{-1}$)
G	molar Gibbs free energy change ($kJ\,kmol^{-1}$)
$\tilde{G}$	dimensionless Gibbs free energy change
h	heat transfer coefficient ($W\,m^{-2}\,K^{-1}$)
$\tilde{h}$	dimensionless heat transfer coefficient
$H_i(T_i)$	molar enthalpy of formation at a temperature T_i of reactants and products ($kJ\,kmol^{-1}$)
$\tilde{H}_i(\theta_i)$	dimensionless molar enthalpy of formation at a dimensionless temperature θ_i of reactants and products
$i_{o,a}$, $i_{o,c}$	exchange current densities ($A\,m^{-2}$)
$i_{lim,a}$, $i_{lim,c}$	limiting current densities ($A\,m^{-2}$)
I	current (A)
$\tilde{I}$	dimensionless current
j	mass flux ($kg\,s^{-1}\,m^{-2}$)
k	thermal conductivity ($W\,m^{-1}\,K^{-1}$)
$\tilde{k}$	dimensionless thermal conductivity
K	permeability (m^2)
L	length (m)
L_{ch}, L_t	gas channels internal dimensions as shown in Fig. 1 (m)
L_x, L_y, L_z	fuel cell length, width and height, respectively (m)
$\dot{m}$	mass flow rate ($kg\,s^{-1}$)
M	molecular weight ($kg\,kmol^{-1}$)
n	equivalent electron per mole of reactant (equiv. mol^{-1})
$\dot{n}$	molar flow rate ($kmol\,s^{-1}$)
n_{ch}	number of parallel ducts in gas channel
N	dimensionless global wall heat transfer coefficient
p	pressure ($N\,m^{-2}$)
P	dimensionless pressure
PEMFC	polymer electrolyte membrane fuel cell
Pr	Prandtl number ($\mu c_p\,K^{-1}$)
q	tortuosity
Q	reaction quotient
$\dot{Q}$	heat transfer rate (W)
$\tilde{Q}$	dimensionless heat transfer rate
r	pore radius (m)
R	ideal gas constant ($kJ\,kg^{-1}\,K^{-1}$)
$\bar{R}$	universal gas constant 8.314 ($kJ\,kmol^{-1}\,K^{-1}$)
Re_h	Reynolds number based on (D_h, $uD_h\rho/\mu$)
S	dimensionless conversion factor, Eq. (37)
t	time (s)
T	temperature (K)
u	mean velocity ($m\,s^{-1}$)
$\tilde{u}$	dimensionless mean velocity
U	global wall heat transfer coefficient ($W\,m^{-2}\,K^{-1}$)
V	voltage (V)
V_T	total volume (m^3)
$\tilde{V}$	dimensionless voltage
$\tilde{V}_T$	dimensionless total volume
$\tilde{W}$	dimensionless fuel cell electrical power
$\tilde{W}_{net}$	dimensionless fuel cell net power, Eq. (33)
$\tilde{W}_{net,s}$	dimensionless fuel cell steady state net power output
$\tilde{W}_p$	dimensionless required pumping power, Eqs. (33) and (36)
[ ]	molar concentration of a substance ($mol\,l^{-1}$)

Greek symbols

α_a, α_c	anode and cathode charge transfer coefficients
β	electrical resistance (Ω)
γ	specific heat ratio
δ	gas channel aspect ratio
ζ	stoichiometric ratio
η_a, η_c	anode and cathode charge transfer overpotentials (V)
$\eta_{d,a}$, $\eta_{d,c}$	anode and cathode mass diffusion overpotentials (V)
$\tilde{\eta}_a$, $\tilde{\eta}_c$	dimensionless anode and cathode charge transfer overpotentials
$\tilde{\eta}_{d,a}$, $\tilde{\eta}_{d,c}$	dimensionless anode and cathode mass diffusion overpotentials
$\tilde{\eta}_{ohm}$	dimensionless fuel cell total ohmic potential loss
θ	dimensionless temperature
λ	ionomer water content
μ	viscosity (Pa s)
ν	reaction coefficients
ξ	dimensionless length
ϕ	porosity
ρ	density ($kg\,m^{-3}$)
$\tilde{\rho}$	dimensionless density
σ	electrical conductivity ($\Omega^{-1}\,m^{-1}$)
τ	dimensionless time
ψ	dimensionless mass flow rate

Subscripts

a	anode
(aq)	aqueous solution
c	cathode
cond	heat conduction

conv	heat convection
CV	control volume
e	reversible
f	fuel
(g)	gaseous phase
h	hydraulic
H^+	hydrogen cation
H_2	hydrogen
H_2O	water
in	control volume inlet
j	control volume index
k	control volume index
(l)	liquid phase
m	one-way maximum
mm	two-way maximum
ohm	ohmic
opt	optima
out	control volume outlet
ox	oxidant
O_2	oxygen
p	polymer electrolyte membrane
ref	reference
sa	anode solid side
sc	cathode solid side
su	start-up
w	wall
wet	wetted surface
0	initial condition
1, . . ., 7	control volume index
12	interaction between CV1 and CV2
23	interaction between CV2 and CV3
34	interaction between CV3 and CV4
45	interaction between CV4 and CV5
56	interaction between CV5 and CV6
67	interaction between CV6 and CV7
∞	ambient

Superscript

0	standard conditions [gases at 1 atm, 25 °C, species in solution at 1*M*, where *M* is the molarity = (moles solute)/(liters solution)]

two phase flow mathematical model with consideration of existing multi-phase water in the flow fields. Those models are expensive to solve numerically, due to the partial difference equations, and to the large number of flow configurations to be tested in an optimization procedure. At the PEMFC stack level, Amphlett et al. [9] introduced a transient mathematical model for predicting the response and performance of the system for applications where the operating conditions change with time, considering heat losses, changes in stack temperature, reactant gas concentrations, and other internal phenomena, but no consideration was given to the pressure drops experienced by the fuel and oxidant in the feeding headers and gas channels. Experimental results were presented by Hamelin et al. [10] for the time response of a stationary PEMFC stack under fast load commutations, and compared to the Amphlett et al. [9] model with good agreement. Several other experimental studies have been conducted to access the dynamic behavior of PEMFC stacks in search for performance improvement in the transient mode [11–15]. Recent studies presented PEMFC stack steady state mathematical models to predict performance [16–18]: one study [18] presented a genetic algorithm technique for finding the best configuration of the stack in terms of number of cells and cell surface area, but did not consider headers and gas channels pumping power losses. No transient model was found in the literature that addresses the spatial temperature and pressure gradients in a PEMFC stack, pressure drops in the headers and single cells gas channels and their effect on performance, with the exception of a recent study published by Vargas et al. [19].

As a result, for the fuel cell structure optimization, it is desirable that the model is as simple as possible, in order to require low computational time to provide solutions for each tested configuration, thus allowing for an effective optimization procedure. With such objectives in mind, Vargas and Bejan [20], and Vargas et al. [21] presented a lumped control volume model for alkaline and PEM fuel cells, respectively, which calculated the fuel cell thermal-fluid field, mass transport mechanism, electrochemical properties, and power consumption and generation. The optimal fuel cell geometry, including internal layer thickness allocation and external aspect ratios, were also obtained in those studies.

In this paper, we amend the model introduced by Vargas et al. [21] and extend the flow structure optimization procedure to multi-objective PEMFC optimization involving the steady state and transient behaviors. The spatial temperature and pressure gradients in a single PEMFC, pressure drops in the cell gas channels, and their effect on performance are investigated. The multi-objective optima according to constructal theory [22] are also discussed in this paper.

2. Thermodynamic model

A thermo-electrochemical model for a single PEM fuel cell operating at steady state has been introduced in a previous study by Vargas et al. [21]. In this study, that mathematical model is amended to study the PEM fuel cell transient performance. According to Vargas et al. [21], the fuel cell is divided into seven control volumes that are shown in Fig. 1. These control volume (CV) interact energetically with one another. The fuel cell also interacts with adjacent fuel cells in a stack, and/or with the ambient. Additionally, two bipolar plates (interconnects) have the function of allowing the electrons produced by the electrochemical oxidation reaction at the anode to flow to the external circuit or to an adjacent cell. The control volumes are the fuel channel (CV1), the anode diffusion-backing layer (CV2), the anode reaction layer (CV3), the polymer electrolyte membrane (CV4), the cathode reaction layer (CV5), the cathode diffusion backing layer (CV6) and the oxidant channel (CV7).

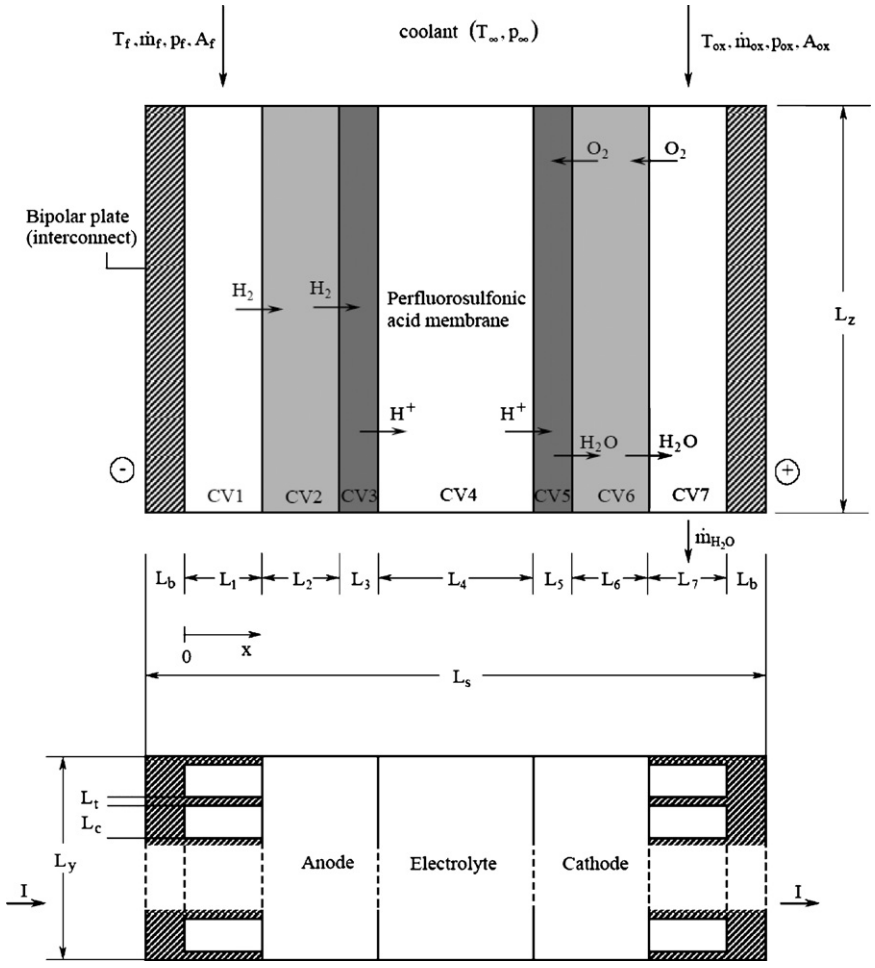

Fig. 1. PEM fuel cell internal structure and external shape.

The model consists of the conservation equations for each control volume, and the equations accounting for electrochemical reactions, where reactions are present. The reversible electrical potential and power of the fuel cell are then computed (based on the reactions) as functions of the temperature and pressure fields determined by the model. The actual electrical potential and power of the fuel cell are obtained by subtracting from the reversible potential the losses due to surface overpotentials (poor electrocatalysis), slow diffusion and all internal ohmic losses through the cell (resistance of individual cell components, including electrolyte layer, interconnects and any other cell components through which electrons flow). These are functions of the total cell current (I), which is directly related to the external load (or the cell voltage). In sum, the total cell current is considered an independent variable in this study.

2.1. Dimensionless variables

To make the results general, this model and its simulation results are formulated and reported in a dimensionless way. The dimensionless variables are defined based on the geometric and operating conditions of the PEM fuel cell.

The dimensionless length ξ and dimensionless area $\tilde{A}$ are defined as

$$\xi = \frac{L}{V_T^{1/3}}, \qquad \tilde{A} = \frac{A}{V_T^{2/3}} \tag{1}$$

where $V_T = L_x L_y L_z$, is the total fuel cell volume.

Pressures and temperatures are referred to ambient conditions: $P = p/p_\infty$ and $\theta = T/T_\infty$. The dimensionless mass flow rates are defined as follows:

$$\psi_i = \frac{\dot{m}_i}{\dot{m}_{ref}} \tag{2}$$

where the subscript i indicates the reactant or product that flows through the fuel cell; and $\dot{m}_{ref}$ is a specified reference mass flow rate given in Table 1. The reference time t_{ref} depends on the reference mass flow rate $\dot{m}_{ref}$, and therefore, the dimensionless time τ and reference time t_{ref} are expressed as follows:

$$\tau = \frac{t}{t_{ref}}, \qquad t_{ref} = \frac{p_\infty V_T}{R_f T_\infty \dot{m}_{ref}} \tag{3}$$

where the subscript "f" stands for fuel. In this paper, for simplicity, we assume that the fuel stream is pure hydrogen, and the oxidant is pure oxygen.

Table 1
Properties and constant values used in the simulations

$B = 0.156$
$c_{p,\mathrm{f}} = 14.95\,\mathrm{kJ\,kg^{-1}\,K^{-1}}$
$c_{p,\mathrm{ox}} = 0.91875\,\mathrm{kJ\,kg^{-1}\,K^{-1}}$
$c_{v,\mathrm{f}} = 10.8\,\mathrm{kJ\,kg^{-1}\,K^{-1}}$
$c_{v,\mathrm{ox}} = 0.659375\,\mathrm{kJ\,kg^{-1}\,K^{-1}}$
$c_{v,\mathrm{sa}} = c_{v,\mathrm{sc}} = 133\,\mathrm{J\,kg^{-1}\,K^{-1}}$
$C_{\mathrm{sol}} = 4180\,\mathrm{J\,kg^{-1}\,K^{-1}}$
$F = 96{,}500\,\mathrm{C\,mol^{-1}}$
$i_{0,\mathrm{a}} = i_{0,\mathrm{c}} = 10\,\mathrm{A\,m^{-2}}$
$I_{\mathrm{ref}} = 1\,\mathrm{A}$
$k_{\mathrm{f}} = 0.2\,\mathrm{W\,m^{-1}\,K^{-1}}$
$k_{\mathrm{ox}} = 0.033\,\mathrm{W\,m^{-1}\,K^{-1}}$
$k_{\mathrm{p}} = 0.21\,\mathrm{W\,m^{-1}\,K^{-1}}$
$k_{\mathrm{s,a}} = k_{\mathrm{s,c}} = 71.6\,\mathrm{W\,m^{-1}\,K^{-1}}$
$K_2 = K_6 = 4 \times 10^{-14}\,\mathrm{m^2}$
$K_3 = K_5 = 4 \times 10^{-16}\,\mathrm{m^2}$
$\dot{m}_{\mathrm{ref}} = 10^{-4}\,\mathrm{kg\,s^{-1}}$
$p_{\mathrm{f}} = p_{\infty} = 0.1\,\mathrm{MPa}$
$p_{\mathrm{ox}} = 0.12\,\mathrm{MPa}$
$q = 1.5$
$R_{\mathrm{f}} = 4.157\,\mathrm{kJ\,kg^{-1}\,K^{-1}}$
$R_{\mathrm{ox}} = 0.2598\,\mathrm{kJ\,kg^{-1}\,K^{-1}}$
$T_{\mathrm{f}} = T_{\mathrm{ox}} = T_{\infty} = 298.15\,\mathrm{K}$
$U_{\mathrm{w}i} = 50\,\mathrm{W\,m^{-2}\,K}$, $i = 1, 7$
$V_{\mathrm{ref}} = 1\,\mathrm{V}$
$V_{\mathrm{T}} = 2.25 \times 10^{-5}\,\mathrm{m^3}$
$V_{\mathrm{T,ref}} = 10^{-5}\,\mathrm{m^3}$
$\alpha_{\mathrm{a}} = \alpha_{\mathrm{c}} = 0.5$
$\phi_2 = \phi_6 = 0.4$
$\phi_3 = \phi_5 = 0.2$
$\mu_1 = 10^{-5}\,\mathrm{Pa\,s}$
$\mu_7 = 2.4 \times 10^{-5}\,\mathrm{Pa\,s}$
$\sigma_1, \sigma_7 = 1.388 \times 10^6\,\Omega^{-1}\,\mathrm{m^{-1}}$
$\sigma_2, \sigma_6 = 4000\,\Omega^{-1}\,\mathrm{m^{-1}}$

Other variables are the nondimensional global wall heat transfer coefficient N, heat transfer coefficient $\tilde{h}$, thermal conductivity $\tilde{k}$, density $\tilde{\rho}$ and specific heat ratio γ, defined as follows:

$$N = \frac{U_{\mathrm{w}} V_{\mathrm{T}}^{2/3}}{\dot{m}_{\mathrm{ref}} c_{p,\mathrm{f}}}, \qquad \tilde{h} = \frac{h V_{\mathrm{T}}^{2/3}}{\dot{m}_{\mathrm{ref}} c_{p,\mathrm{f}}}, \qquad \tilde{k} = \frac{k V_{\mathrm{T}}^{1/3}}{\dot{m}_{\mathrm{ref}} c_{p,\mathrm{f}}},$$
$$\tilde{\rho} = \frac{\rho R_{\mathrm{f}} T_{\infty}}{p_{\mathrm{f}}}, \qquad \gamma = \frac{c_{p,\mathrm{f}}}{c_v} \tag{4}$$

where $c_{p,\mathrm{f}}$ is the fuel specific heat at constant pressure.

The reference energy flow rate is defined by $\dot{E}_{\mathrm{ref}} = \dot{m}_{\mathrm{ref}} c_{p,\mathrm{f}} T_{\infty}$, which is used as a reference scale for power related variables:

$$(\Delta\tilde{E}, \Delta\tilde{E}_{\mathrm{CV}}, \tilde{Q}, \Delta\tilde{H}, \Delta\tilde{G}) = \frac{(\Delta\dot{E}, \Delta\dot{E}_{\mathrm{CV}}, \dot{Q}, \Delta\dot{H}, \Delta\dot{G})}{\dot{E}_{\mathrm{ref}}} \tag{5}$$

The dimensionless heat transfer rates are given by

$$\tilde{Q}_{\mathrm{conv}} = \tilde{h}\tilde{A}\Delta\theta, \qquad \tilde{Q}_{\mathrm{cond}} = \frac{-\tilde{k}\tilde{A}\Delta\theta}{\xi}, \qquad \tilde{Q}_{\mathrm{w}} = N\tilde{A}_{\mathrm{w}}\Delta\theta,$$
$$\tilde{Q}_{\mathrm{ohm}} = \frac{I^2\beta}{\dot{m}_{\mathrm{ref}} c_{p,\mathrm{f}} T_{\infty}} \tag{6}$$

where β is the electrical resistance.

The physics of the fuel cell is described by taking into account the mass conservation and the first law of thermodynamics at each CV, and the electrochemical reactions at CV3 and CV5.

2.2. Mass balance

The hydrogen mass flow rate required by the working current (I), which indicates the external load, is given by

$$\dot{m}_{\mathrm{H_2}} = \dot{n}_{\mathrm{H_2}} M_{\mathrm{H_2}} = \frac{I}{nF} M_{\mathrm{H_2}} \tag{7}$$

where $\dot{n}_{\mathrm{H_2}}$ is the molar flow rate for hydrogen; $M_{\mathrm{H_2}}$ the molecular weight of hydrogen; n the equivalent electron per mole of reactant, equiv. $\mathrm{mol^{-1}}$ ($n = 2$); and F is the Faraday constant, 96,500 C equiv.$^{-1}$.

Similarly, the oxygen mass flow rate needed in the PEM fuel cell electrochemical reaction is evaluated as follows:

$$\dot{m}_{\mathrm{O_2}} = \frac{1}{2}\dot{n}_{\mathrm{H_2}} M_{\mathrm{O_2}} \tag{8}$$

The stoichiometric ratios, denoted as ζ_1 on the fuel side and ζ_7 on the oxidant side, are defined as the provided reactant divided by the reactant needed for the electrochemical reaction of interest and greater than 1. The stoichiometric ratios are the design constraints of this study. Therefore, considering the stoichiometric ratios, the dimensionless inlet reactant mass flow rates are $\psi_{\mathrm{f}} = \zeta_1\psi_{\mathrm{H_2}} = \zeta_1\dot{m}_{\mathrm{H_2}}/\dot{m}_{\mathrm{ref}}$ and $\psi_{\mathrm{ox}} = \zeta_7\psi_{\mathrm{O_2}} = \zeta_7\dot{m}_{\mathrm{O_2}}/\dot{m}_{\mathrm{ref}}$, where $\dot{m}_{\mathrm{H_2}}$ and $\dot{m}_{\mathrm{O_2}}$ are obtained from Eqs. (7) and (8).

2.3. Energy conservation

The thermal model consists of coupled ordinary differential equations that are obtained from the energy conservation principle applied to each control volume, as shown in Fig. 1. The energy conservation in CV1 is expressed as follows:

$$\tilde{Q}_{\mathrm{w1}} + \psi_{\mathrm{f}}(\theta_{\mathrm{f}} - \theta_1) + \tilde{Q}_{12} + \tilde{Q}_{\mathrm{ohm1}} = \frac{1}{\dot{E}_{\mathrm{ref}}}\frac{\mathrm{d}E_{\mathrm{CV1}}}{\mathrm{d}t} \tag{9}$$

where $\tilde{Q}_{\mathrm{w1}} = N_1\tilde{A}_{\mathrm{w1}}(1 - \theta_1)$, stands for the heat transfer rate from the ambient to the CV1 through the wall. The wall surface connecting the CV$_j$ ($j = 1, 7$) and the ambient ($\tilde{A}_{\mathrm{w}j}$) is calculated by $\tilde{A}_{\mathrm{w}j} = \xi_y\xi_z + 2(\xi_y + \xi_z)\xi_j$. The second term in the left hand side of Eq. (9) is the dimensionless fuel enthalpy decrease, which is obtained by assuming that the reactant leaves the fuel cell at the CV1 temperature. $\tilde{Q}_{12} = \tilde{h}_1\tilde{A}_{\mathrm{s}}(1 - \phi_2)(\theta_2 - \theta_1)$ denotes the heat transfer rate from CV2 to CV1. The fuel cell cross-sectional area is $\tilde{A}_{\mathrm{s}} = \xi_y\xi_z$. The heat transfer coefficients h_j ($j = 1, 7$) in the gas channels are estimated according to the flow regime. For the laminar flow ($Re_{\mathrm{h}} < 2300$) [23]:

$$\frac{h_j D_{\mathrm{h},j}}{k_j} = 7.541(1 - 2.610\delta_j + 4.970\delta_j^2 - 5.119\delta_j^3 + 2.702\delta_j^4 - 0.548\delta_j^5), \quad j = 1, 7 \tag{10a}$$

For the turbulent flow ($2300 < Re_h < 2 \times 10^4$) [24]:

$$\frac{h_j D_{h,j}}{k_j} = \frac{(f_j/2)(Re_{h,j} - 1000)Pr_j}{1 + 12.7(f_j/2)^{1/2}(Pr_j^{2/3} - 1)}, \ j = 1, 7 \tag{10b}$$

where $\delta_j = L_{ch}/L_j$, for $L_{ch} \le L_j$ and $\delta_j = L_j/L_{ch}$, for $L_{ch} > L_j$; $D_{h,j} = 2L_{ch}L_j/(L_{ch} + L_j)$; Pr is the gas Prandtl number; and f is the friction factor given by $f_j = 0.079\,\mathrm{Re}_{h,j}^{-1/4}$ when $2300 < Re_{h,j} < 2 \times 10^4$ [24].

The Reynolds number is a function of the gas flow velocity u_j. According to Vargas et al. [21], these velocities are calculated by

$$u_1 = \frac{R_f T_1 \dot{m}_{ref}}{p_f L_{ch} L_1 n_{ch}} \left(\psi_f - \frac{\psi_{H_2}}{2} \right) \tag{11a}$$

$$u_7 = \frac{R_{ox} T_7 \dot{m}_{ox}}{2 p_{ox} L_{ch} L_7 n_{ch}} \left(\psi_{ox} - \frac{\psi_{O_2}}{2} \right) \tag{11b}$$

Finally, the ohmic heating rate $\tilde{Q}_{ohm1} = I^2 \beta_1/(\dot{m}_{ref} c_{p,f} T_\infty)$ with the previous dimensionless energy fluxes contribute to the increase of the interconnect internal energy as follows:

$$\frac{d\theta_1}{d\tau} = \frac{\gamma_f}{n_{ch}\xi_1\xi_c\xi_z} \frac{\theta_{1,0}}{p_f} [\tilde{Q}_{w1} + \psi_f(\theta_f - \theta_1) + \tilde{Q}_{12} + \tilde{Q}_{ohm1}] \tag{12}$$

where $\theta_{1,0}$ is the CV1's initial dimensionless temperature, and $\gamma_f = c_{p,f}/c_{v,f}$ is the fuel gas specific heat ratio. The average fuel pressure (p_f in CV1) and oxidant pressure (p_{ox} in CV7) are assumed known and constants, shown in Table 1, during the fuel cell operation.

The anode backing diffusion layer (CV2) is porous, which consists of a solid side and a fluid side. The mass of fluid in CV2 is negligible compared to the mass of solid. Therefore, the CV2 internal energy differential is $dE_{CV2} = m_{CV2} c_{v,sa} dT_2$. The net heat transfer rate through CV2 is $\tilde{Q}_2 = -\tilde{Q}_{12} + \tilde{Q}_{w2} + \tilde{Q}_{23} + \tilde{Q}_{ohm2}$, where $\tilde{Q}_{23} = -\tilde{k}_{sa}(1 - \phi_2)\tilde{A}_s(\theta_2 - \theta_3)/[(\xi_2 + \xi_3)/2]$. The anode solid side dimensionless thermal conductivity $\tilde{k}_{sa}$ was defined in Eq. (4). The energy balance in CV2 leads to the CV2's dimensionless temperature expression as follows:

$$\frac{d\theta_2}{d\tau} = \frac{\gamma_{sa}}{\tilde{\rho}_{sa}(1 - \phi_2)\xi_2\xi_y\xi_z} [\psi_{H_2}(\theta_1 - \theta_2) + \tilde{Q}_2] \tag{13}$$

where $\tilde{\rho}_{sa}$is the dimensionless density of the anode solid side, and γ_{sa} is the effective specific heat ratio of the anode solid side.

The flow in the electrodes is modeled as Knudsen flow [25]. The fuel and oxidant mass fluxes are given by

$$j_j = -[D(\rho_{out} - \rho_{in})/L]_j, \ j = 2, 6 \tag{14}$$

where $D = B\{r[8\bar{R}T/(\pi M)^{1/2}\phi^q\}$ is the Knudsen diffusion coefficient; ρ the density; $\bar{R}$ the universal gas constant; ϕ the porosity; q the tortuosity [26,27]; B is a correction coefficient. By using Eq. (14) and the ideal gas model for H_2 and O_2, we find the pressures of the hydrogen and oxygen that enter the catalyst layers as follows:

$$P_{j,out} = P_{j,in} - \frac{j_j R_k T_\infty L_j \theta_j}{D_j p_\infty}, \ j = 2, 6; \ k = f, ox \tag{15}$$

where $j_2 = \dot{m}_{H_2}/A_{3,wet}$, and $j_3 = \dot{m}_{O_2}/A_{5,wet}$. $A_{3,wet}$ and $A_{5,wet}$ are the wetted surface areas in the porous catalyst layers, defined as $A_{wet,j} = 4\phi_j L_j K_j^{-1/2} A_s$, $j = 3, 5$, where K is the permeability and ϕ is the porosity. Because the channel layer is structurally connected to CV2 and CV6, we assume that $P_{2,in} = P_f$ and $P_{6,in} = P_{ox}$. The average pressures in CV2 and CV6 are estimated as follows:

$$P_j = \frac{1}{2}(P_{j,in} + P_{j,out}), \ j = 2, 6 \tag{16}$$

In the reaction layer (CV3), there are a few considerations that must be taken into account in the energy balance. An oxidation reaction, $H_{2(g)} \rightarrow 2H_{(aq)}^+ + 2e^-$, takes place in this layer. The dimensionless molar enthalpy change due to the reaction is given by $-\Delta\tilde{H}_3 = \sum_{reactants}[\nu_j \tilde{H}_j(T_j)] - \sum_{products}[\nu_j \tilde{H}_j(T_j)]$. Here, ν_j is the reaction coefficient. $\tilde{H}_j$ is the dimensionless molar enthalpy of formation of component j [28,29]. The dimensionless reversible electrical power, $\tilde{W}_{e3}$, is expressed in terms of the dimensionless Gibbs free energy change, i.e., $\tilde{W}_{e3} = -\Delta\tilde{G}_3$, which is also part of the CV3's energy balance. The Gibbs free energy change, ΔG_3, is a function of the temperature and pressure as follows:

$$\Delta G_j = \Delta G_j^\circ + \bar{R} T_j \ln Q_j, \ j = 3, 5 \tag{17}$$

where ΔG_3° is the standard Gibbs free energy change (kJ kmol^{-1}); Q is the reaction quotient and is formulated by $Q_3 = [H_{(aq)}^+]^2/p_{H_2}$; $[H_{(aq)}^+]$ is the molar concentration of the acid solution (mol/l); and $p_{H_2} = p_{2,out}$ is the partial pressure of H_2 at the CV2 outlet. Recall that the pure liquids or solids do not appear in the calculation of Q_3, neither does the solvent in a dilute solution, $[H_{(aq)}^+]$ is a function of water content λ, i.e., $[H_{(aq)}^+] \approx \rho_{H_2O}/\lambda_4 M_{H_2O}$ for a dilute water solution.

The dimensionless net heat flux flowing in CV3 is given by $\tilde{Q}_3 = -\tilde{Q}_{23} + \tilde{Q}_{w3} + \tilde{Q}_{34} + \tilde{Q}_{ohm3}$. Since the heat transfer rate between CV3 and CV4 (the polymer electrolyte membrane) is dominated by conduction, therefore, this dimensionless heat flux is $\tilde{Q}_{34} = -2(1 - \phi_3)(\theta_3 - \theta_4)\tilde{A}_s\tilde{k}_{sa}\tilde{k}_p/(\xi_4\tilde{k}_{sa} + \xi_3\tilde{k}_p)$.

Considering the solid compartment dominates the electrode mass, the mass and energy balance analysis in CV3 leads to a dimensionless temperature expression as follows:

$$\frac{d\theta_3}{d\tau} = \frac{\gamma_{sa}}{\tilde{\rho}_{sa}(1 - \phi_3)\xi_3\xi_y\xi_z} [\tilde{Q}_3 - \Delta\tilde{H}_3 + \Delta\tilde{G}_3] \tag{18}$$

where $(\Delta\tilde{H}_3, \Delta\tilde{G}_3) = \dot{n}_{H_2}(\Delta H_3, \Delta G_3)/(\dot{m}_{ref} c_{p,f} T_\infty)$, $\dot{n}_{H_2} = \dot{m}_{H_2}/M_{H_2}$, and other parameters are similar to CV2 discussion.

The polymer electrolyte membrane (CV4) interacts with CV3, CV5 and the ambient. In the cathode reaction layer (CV5), there occurs the reaction expressed by $\frac{1}{2}O_{2(g)} + 2e^- + 2H_{(aq)}^+ \rightarrow H_2O_{(l)}$. Considering the mass conservation in CV4 and other control volumes in the fuel cell, we have $2\dot{n}_{H_2} = \dot{n}_{H_{out}^+} = \dot{n}_{H_{in}^+} = 2\dot{n}_{O_2}$. In conclusion, $\dot{n}_{O_2} = \dot{n}_{H_2}$, where $\dot{n}_{O_2} = 2\dot{m}_{O_2}/M_{O_2}$. Accordingly, the required oxidant mass flow rate is $\dot{m}_{O_2} = \dot{m}_{H_2} M_{O_2}/2M_{H_2}$. The dimensionless net heat transfer in CV4 is obtained from $\tilde{Q}_4 = -\tilde{Q}_{34} + \tilde{Q}_{w4} + \tilde{Q}_{45} + \tilde{Q}_{ohm4}$ and $\tilde{Q}_{45} = -2(1 - \phi_5)(\theta_4 - \theta_5)\tilde{A}_s\tilde{k}_{sa}\tilde{k}_p/(\xi_4\tilde{k}_{sc} + \xi_5\tilde{k}_p)$. Then,

the CV4 dimensionless temperature is obtained from

$$\frac{d\theta_4}{d\tau} = \frac{\gamma_p}{\tilde{\rho}_p \xi_4 \xi_y \xi_z}\left[\tilde{Q}_4 + \tilde{H}(\theta_3)_{H_{(aq)}{}^+} - \tilde{H}(\theta_4)_{H_{(aq)}{}^+}\right] \quad (19)$$

where $\tilde{\rho}_p$ is the dimensionless density of membrane solution, and γ_p is the effective specific heat ratio of the polymer electrolyte membrane.

The analysis in the cathode reaction layer (CV5) is analogous to what we previously presented in the anode reaction layer (CV3) analysis. The CV5 dimensionless temperature is obtained by

$$\frac{d\theta_5}{d\tau} = \frac{\gamma_{sc}}{\tilde{\rho}_{sc}(1-\phi_5)\xi_5 \xi_y \xi_z}[\tilde{Q}_5 - \Delta\tilde{H}_5 + \Delta\tilde{G}_5] \quad (20)$$

where $(\Delta\tilde{H}_5, \Delta\tilde{G}_5) = \dot{n}_{O_2}(\Delta H_5, \Delta G_5)/(\dot{m}_{ref} c_{p,f} T_\infty)$, $\dot{n}_{O_2} = \dot{m}_{H_2}/2M_{H_2}$, $\dot{n}_{H_2O,out} = \dot{n}_{O_2}\tilde{\rho}_{sc}$ is the dimensionless density of the cathode solid side, and γ_{sc} is the effective specific heat ratio of the cathode solid side.

Similarly, the dimensionless net heat transfer rate flowing in CV5 is given by $\tilde{Q}_5 = -\tilde{Q}_{45} + \tilde{Q}_{w5} + \tilde{Q}_{56} + \tilde{Q}_{ohm5}$, with $\tilde{Q}_{56} = -2\tilde{k}_{sc}\tilde{A}_s(1-\phi_6)(\theta_5-\theta_6)/(\xi_5+\xi_6)$. The molar enthalpy change $\left(\Delta H_5 = \sum_{products}[\nu_j H_j(T_j)] - \sum_{reactants}[\nu_j H_j(T_j)]\right)$ indicates the reaction heat production (kJ kmol^{-1}); ν_j are the reaction coefficients. $H_j(T_j)$ is the formation enthalpy (kJ kmol^{-1}) at a temperature T_j of compound j in reactants and products. The enthalpies of formation are obtained from tabulated values [28,29] at T_6 for $O_{2(g)}$ and T_4 for $H_{(aq)}{}^+$, and T_5 for $H_2O_{(l)}$ at 1 atm, respectively. The change in the Gibbs free energy, ΔG_5, is calculated by Eq. (17). The CV5 reaction quotient is $Q_5 = \{[H_{(aq)}{}^+]^2 p_{O_2}^{1/2}\}^{-1}$, where $p_{O_2} = p_{6,out}$.

The mass balance for CV6 yields $\dot{m}_{O_2,out} = \dot{m}_{O_2,in} = \dot{m}_{O_2}$ and $\dot{n}_{H_2O} = \dot{n}_{H_2O,out} = \dot{n}_{H_2O,in} = \dot{n}_{O_2}$. The dimensionless net heat transfer rate in CV6 results from $\tilde{Q}_6 = -\tilde{Q}_{56} + \tilde{Q}_{w6} + \tilde{Q}_{67} + \tilde{Q}_{ohm6}$, $\tilde{Q}_{67} = \tilde{h}_7\tilde{A}_s(1-\phi_6)(\theta_7-\theta_6)$, $\tilde{h}_7 = h_7 V_T^{2/3}/\dot{m}_{ref} c_{p,f}$. The dimensionless temperature for CV6 is given by

$$\frac{d\theta_6}{d\tau} = \frac{\gamma_{sc}}{\tilde{\rho}_{sc}\xi_y\xi_z\xi_6(1-\phi_6)} \times \left[\tilde{Q}_6 + \psi_{O_2}\frac{c_{p,ox}}{c_{p,f}}(\theta_7-\theta_6) + \tilde{H}(\theta_5)_{H_2O} - \tilde{H}(\theta_6)_{H_2O}\right] \quad (21)$$

The dimensionless net heat transfer rate in CV7 is $\tilde{Q}_7 = -\tilde{Q}_{67} + \tilde{Q}_{w7} + \tilde{Q}_{ohm6}$. The balances for mass and energy in the oxidant channel (CV7), with the assumptions of non-mixing flow and the assumption that the space is filled mainly with dry oxygen, yields $\dot{m}_{H_2O} = \dot{m}_{H_2O,in} = \dot{m}_{H_2O,out} = \dot{n}_{O_2} M_{H_2O}$, and the dimensionless CV7 temperature as follows:

$$\frac{d\theta_7}{d\tau} = \frac{\gamma_{ox} R_{ox}\theta_{7,0}}{P_{ox} n_c \xi_7 \xi_c \xi_z} \times \left[\tilde{Q}_7 + \psi_{ox}\frac{c_{p,ox}}{c_{p,f}}(\theta_{ox}-\theta_7) + \tilde{H}(\theta_6)_{H_2O} - \tilde{H}(\theta_7)_{H_2O}\right]. \quad (22)$$

2.4. Electrochemical model

The thermal model described by Eqs. (12), (13), (18)–(22) needs to be complemented by the electrochemical counterpart such that the PEM fuel cell power generation performance can be calculated. The resistances, $\beta(\Omega)$, of each compartment are evaluated from the material and geometric features as

$$\beta_j = \frac{\xi_j}{\tilde{A}_s V_T^{1/3}\sigma_j(1-\phi_j)}, \quad j = 1, 2, 6, 7 \quad (23)$$

$$\beta_j = \frac{\xi_j}{\tilde{A}_s V_T^{1/3}\sigma_j\phi_j}, \; j = 3, 4, 5, \; \phi_4 = 1 \quad (24)$$

where the ionic conductivity, σ (Ω^{-1} m^{-1}), of Nafion 117 as a function of temperature is given by the following empirical formula [30]:

$$\sigma_j(\theta) = \exp\left[1268\left(\frac{1}{303} - \frac{1}{\theta_j T_\infty}\right)\right](0.5139\lambda_j - 0.326), \quad j = 3, 4, 5 \quad (25)$$

The conductivities of the catalyst layers are given by $\sigma_3\phi_3$ and $\sigma_5\phi_5$, according to Eqs. (24) and (25), which agree qualitatively with previously measured catalyst layers ionic conductivities [31], i.e., the ionic conductivity increases with increasing Nafion content, which increases as ϕ increases in the present model. The conductivities of the diffusive layers, σ_2 and σ_6, are the carbon-phase conductivities [32]. Finally, the conductivities of CV1 and CV7, σ_1 and σ_7, are the electrical conductivities of the bipolar plate material. The CV1 and CV7 void fractions in Eq. (23), i.e., $\phi_1 = \phi_7 = \xi_{ch}/(\xi_t + \xi_{ch})$, are computed for any particular fuel cell internal geometry according to Fig. 1.

In Eq. (25), λ is the water content that is described as the ratio of the number of water molecules to the number of charge sites. In a polymer membrane, the charge sites are ions, $SO_3{}^-H^+$. It is assumed that all ingredients of the catalyst layer are evenly distributed, and that the liquid water product is evenly distributed. Therefore, the water content in ionomer (within the catalyst layer) is assumed constant: this corresponds to the value measured when the ionomer is in contact with liquid water, or to some average between this value and the value corresponding to when the ionomer is in contact with saturated water vapor [33]. Usually, the anode water content is different from that in the cathode; therefore for assumed values of λ_a (anode water content, or λ_3) and λ_c (cathode water content, or λ_5), and by assuming a linear variation of the water content along the membrane thickness, the average water content in the membrane is defined as

$$\lambda_4 = \frac{\lambda_a + \lambda_c}{2} \quad (26)$$

Now, we can calculate the molar concentration of the acid solution $[H_{(aq)}{}^+]$ mentioned in CV3 energy conservation analysis and the ionic conductivity in Eq. (25).

The polarization curve indicates the performance of a fuel cell. The dimensionless potential is defined in terms of a given

reference voltage V_{ref}, namely $\tilde{V} = V/V_{ref}$ and $\tilde{\eta} = \eta/V_{ref}$. The dimensionless actual potential $\tilde{V}$ is an accumulated result of dimensionless anode electrical potential $\tilde{V}_a$, dimensionless cathode electrical potential $\tilde{V}_c$, and the dimensionless ohmic loss ($\tilde{\eta}_{ohm}$) in the space from CV1 to CV7, i.e.,

$$\tilde{V} = \tilde{V}_a + \tilde{V}_c - \tilde{\eta}_{ohm} \tag{27}$$

The ohmic loss $\tilde{\eta}_{ohm}$ is estimated by

$$\tilde{\eta}_{ohm} = \frac{I}{V_{ref}} \sum_{i=1}^{7} \beta_i \tag{28}$$

The actual electrical potential at the anode is $\tilde{V}_a = \tilde{V}_{e,a} - \tilde{\eta}_a - |\tilde{\eta}_{d,a}|$, where the reversible electrical potential at the anode $V_{e,a}$ is given by the Nernst equation [29]:

$$V_{e,a} = V^0_{e,a} - \frac{\bar{R}T_3}{nF} \ln Q_3 \tag{29}$$

where $Q_3 = [H_{(aq)}{}^+]^2/p_{H_2}$ and $V^0_{e,a} = \Delta G^\circ_3/(-nF)$. Mass diffusion and charge transfer cause the potential losses at the anode. The overpotential due to charge transfer (η_a) is obtained from the Bulter–Volmer equation [34,35] as follows:

$$\frac{I}{A_{3,wet}} = i_{o,a} \left[\exp\left(\frac{(1-\alpha_a)\eta_a F}{\bar{R}T_3} \right) - \exp\left(-\frac{\alpha_a \eta_a F}{\bar{R}T_3} \right) \right] \tag{30}$$

where α_a is the anode charge transfer coefficient, and $i_{o,a}$ is the anode exchange current density (a function of catalyst type, catalyst layer morphology, temperature and pressure) , which is listed in Table 1. The potential loss due to mass diffusion [34] is

$$\eta_{d,a} = \frac{\bar{R}T_3}{nF} \ln\left(1 - \frac{I}{A_{wet,3} i_{lim,a}} \right) \tag{31}$$

where the limiting current density at the anode $i_{lim,a}$ occurs at high values of the surface overpotential, when the gas is completely depleted in the very thin active catalyst layer fraction situated at the interface with the gas diffuser, i.e., $P_{2,out} = 0$. Therefore, $i_{lim,a}$ is obtained from Eq. (15), i.e.,

$$i_{lim,a} = \frac{p_f D_2 nF}{M_{H_2} L_2 R_f \theta_2 T_\infty} \tag{32}$$

The methodology in estimating the anode potential is valid in building the cathode potential correlations. Similarly, the actual cathode potential is $\tilde{V}_c = \tilde{V}_{e,c} - \tilde{\eta}_c - |\tilde{\eta}_{d,c}|$ and the reversible electrical cathode potential is $V_{e,c} = V^0_{e,c} - (\bar{R}T_5/nF)\ln(Q_5)$, where $Q_5 = \{[H_{(aq)}{}^+]^2 p_{O_2}^{1/2}\}^{-1}$ and $V^0_{e,c} = \Delta G^\circ_5/(-nF)$. The Butler–Volmer equation for calculating the cathode side overpotential η_c is $I/A_{5,wet} = i_{o,c}[\exp((1-\alpha_c)\eta_c F/\bar{R}T_5) - \exp(-\alpha_c \eta_c F/\bar{R}T_5)]$. The cathode mass diffusion depleting overpotential is $\eta_{d,c} = \bar{R}T_5/nF \ln(1 - I/A_{wet,5} i_{lim,c})$, and the cathode limiting current density is $i_{lim,c} = 2p_{ox} D_6 nF/M_{O_2} L_6 R_{ox} \theta_6 T_\infty$.

2.5. Pumping power and fuel cell net power model

The dimensionless pumping power $\tilde{W}_p$ is required to supply the fuel cell with fuel and oxidant. Therefore, the total net power output (available for utilization) of the fuel cell is

$$\tilde{W}_{net} = \tilde{W} - \tilde{W}_p \tag{33}$$

where $\tilde{W}$ is the total fuel cell electrical power output and $\tilde{W} = \tilde{V}\tilde{I}$. It is necessary to evaluate the pressure drops in the reactant supply channel before estimating the pumping power consumption in the fuel cell. Assuming that the channel is straight and sufficiently slender, the pressure drops are expressed by

$$\Delta P_j = f_j \left(\frac{\xi_z}{\xi_j} + \frac{\xi_z}{\xi_{ch}} \right) \frac{P_j}{\theta_j} \frac{u_j^2}{R_k T_\infty} \tag{34}$$

where $j = 1, 7$ and $k = f$, ox, respectively. The friction factor (f_i) in the gas channels is estimated by experimental correlations from the literature. For the laminar regime ($Re_h < 2300$) we used the correlation [33]:

$$f_j\, Re_{h,j} = 24(1 - 1.3553\delta_j + 1.9467\delta_j^2 - 1.7012\delta_j^3 + 0.9564\delta_j^4 - 0.2537\delta_j^5) \tag{35}$$

where $\delta_j = L_{ch}/L_j$, for $L_{ch} \le L_j$ and $\delta_j = L_j/L_{ch}$, for $L_{ch} > L_j$; $D_{h,j} = 2L_{ch}L_j/(L_{ch} + L_j)$, $Re_{h,j} = u_j D_{h,j} \rho_j/\mu_j$ and $j = 1, 7$. The correlation used for the turbulent regime is the same as the CV1 energy conservation analysis.

Then, the dimensionless pumping power $\tilde{W}_p$ is obtained as follows:

$$\tilde{W}_P = \psi_f S_f \frac{\theta_1}{P_1} \Delta P_1 + \psi_{ox} S_{ox} \frac{\theta_7}{P_7} \Delta P_7 \tag{36}$$

where

$$S_j = \frac{\dot{m}_{ref} T_\infty R_j}{V_{ref} I_{ref}}, \quad j = \text{f, ox.} \tag{37}$$

3. Shape optimization and results

The thermal system reduces to seven nonlinear ordinary differential equations, Eqs. (12), (13), (18)–(22), in which the unknowns are the temperatures of the seven control volumes. A Fortran computational code was written to obtain both steady state and transient solutions. The transient solutions were obtained by solving the system with a Runge-Kutta fourth/fifth order method [36] from a given initial condition. For obtaining steady state results, a system of seven nonlinear algebraic equations was generated by setting the time derivatives equal to 0. The system was then solved with a quasi-Newton method [36]. The Newton iterative process was set to achieve convergence when the Euclidean norm of the residual of the system was less than 10^{-6}. Because of this, the computational time required for one geometric structure study case was short.

In order to make the PEM fuel cell design close to the vehicle application, in this study we conducted a multi-objective optimization procedure to seek the optimal geometric dimension or

limits with the goal of immediate response to step current load and as high as possible steady-state net power output. Table 1 shows the properties and constant values used to produce the numerical results of the present study. The fuel and oxidant inlet temperature were assumed at 298.15 K. The average fuel and oxidant channel pressures were assumed as 1 and 1.2 atm, respectively. Fig. 1 illustrates the main geometric features of the single PEM fuel considered in this study: the external dimensions (L_x, L_y, and L_z), and the individual layer thicknesses (L_i). The geometric constraints of the original study case of this paper are as follows, $\tilde{V}_T = 2.25$, $\xi_y = \xi_z = 160\xi_x$, and $(\xi_1, \xi_2, \xi_3, \xi_4, \xi_5, \xi_6, \xi_7) = (0.05, 0.36, 0.01, 0.06, 0.01, 0.36, 0.05)\xi_x$.

The PEM fuel cell polarization curve indicates that there exists an optimal working current at which the fuel cell has maximal net power output. In this study, we focus on the fuel cell steady-state performance (net power output $\tilde{W}_{net,s}$) and the transient behavior (start-up time t_{su}) characteristics under such optimal working current condition. We also explore the considered geometric dimension effects on those two performance indicators. Fig. 2a and b illustrate a typical transient behavior of a PEM fuel cell in its start-up process. Fig. 2a shows the electrode potentials and the power output compartments in the transient process responding to a step-changed current load. Fig. 2b shows the dimensionless temperature transient process after a step-changed current load applied to the fuel cell. Considering the power support purpose of the PEM fuel cell, the transient behavior indicator, the start-up time, is defined as the time when the net power output arrived at 98% of its steady-state power output. This measurement takes into account two phenomena of PEM fuel cell transient behavior shown in Fig. 2a and b: (i) electrical properties (e.g. voltages, net power output) respond more quickly than the thermal properties (e.g. temperature) – there are power and voltage jumps in the beginning of the transient process, while the temperatures of each component of fuel cell increase slowly and continuously because of high thermal inertia of porous media and the reactants – this phenomenon is quite similar to the conventional internal combustion engine that supplies the power requirement almost immediately, but arrives to its thermal steady state quite slowly, and (ii) after the net power output reaches 98% of its steady-state power level, the net power output curve's slope is close to 0, while the fuel cell temperatures are still increasing—in other words, after a certain period of the transient process, the thermal mechanisms (e.g. temperatures) do not affect significantly the PEM fuel cell power generation. Therefore, it is questionable to consider the transient period as the start-up time based on temperature stabilization.

Fig. 3 demonstrates that the electrode reaction layer thicknesses (ξ_3 and ξ_5) are crucial to PEM fuel cell transient process which can be categorized into three modes, i.e. "under-powered", "exact-powered", and "over-powered". When the electrode reaction thickness is small, say smaller than $0.003\xi_x$, the transient process is "over-powered", while the net power output jumps higher than the steady-state net power output and then decreases to the steady-state net power output level. When the electrode reaction layer thickness is increased to $0.007\xi_x$, the net power output reaches the steady-state level immediately, named as "exact-powered" transient process. When the electrode

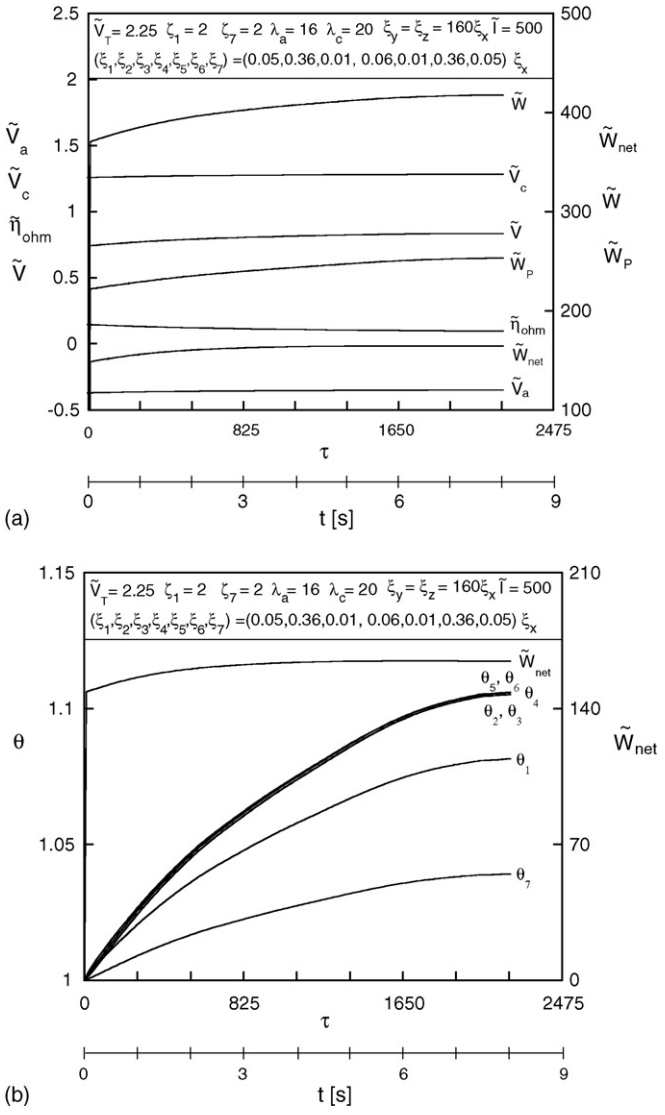

Fig. 2. Polarization and power curves with respect to time (a), and net power and internal temperature vs. time (b).

reaction layer thickness exceeds this critical value, the transient process will be "under-powered" and the net power output increases to the steady-state level continuously after the beginning jump. Fig. 3 was constructed in a way to show clearly the three transient operation modes, but it should be noted that $W_{net,s}$ is strongly dependent on the reaction layer thickness, which is the subject of discussion in Fig. 4.

Fig. 4 shows the comparison of the PEM fuel cell steady-state performance, the steady-state net power output, and the transient behavior, i.e., the start-up time. The PEM fuel cell shows maximum steady-state net power output and short start-up time of "over-powered" process at $\xi_3 = \xi_5 = 0.003\xi_x$. It is the multi-objective optimization design of the electrode reaction layer for the PEM fuel cell and the first level of optimization in this study, named one-way optimization. In the "under-powered" range, ξ_3, $\xi_5 > 0.007\xi_x$, the steady-state net power output decreases dramatically, and the start-up time increases considerably, therefore affecting negatively the two objective functions.

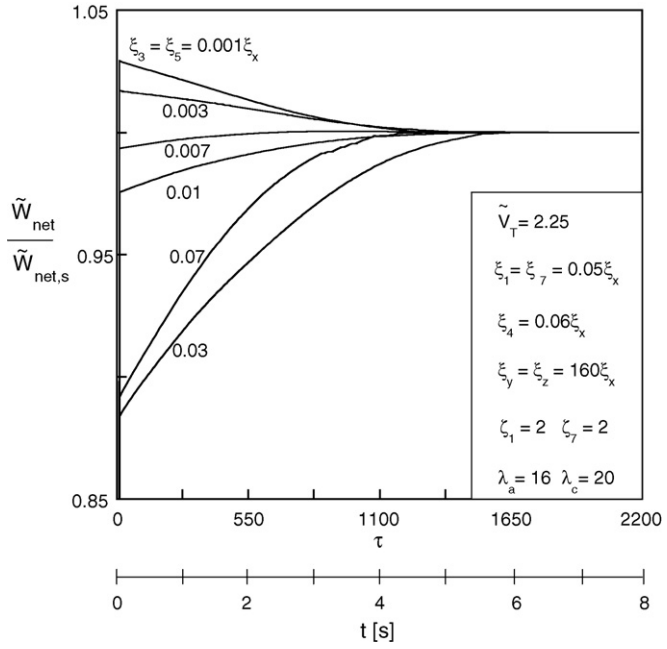

Fig. 3. The normalized net power output of PEMFC transient response.

A fixed internal geometric parameter is the thickness (ξ_4) of the polymer electrolyte membrane. The optimization of the electrode reaction layers thickness was conducted for several values of ξ_4, which produces the results shown in Fig. 5. It is observed that the transient process is in the "over-powered" or "exact-powered" modes, and the start-up time is close to 0, when ξ_4/ξ_x is smaller than 0.08. When the membrane thickness exceeds such critical ratio, the transient process deteriorates dramatically, and the start-up time increases abruptly. In the entire range of the membrane thickness studied, the steady-state net power output decreases monotonically as the membrane thickness increases because of the increment of proton transport resistance in the membrane and the drop of the membrane ionic conductivity. The start-up time curve is unimodal and approaches 0 when $\xi_4/\xi_x \leq 0.08$ due to the small electrical inertia and the low electrical resistance. When $\xi_4/\xi_x > 0.08$, the start-up time increases drastically and reaches a maximum value at $\xi_4/\xi_x = 0.2$ because

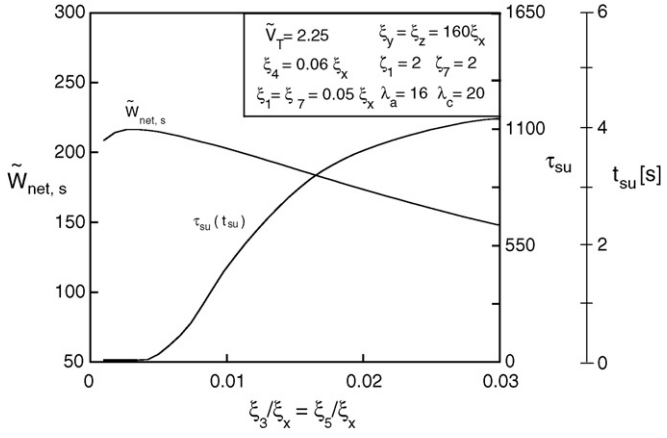

Fig. 4. The one-way net power maximization for optimal internal structure.

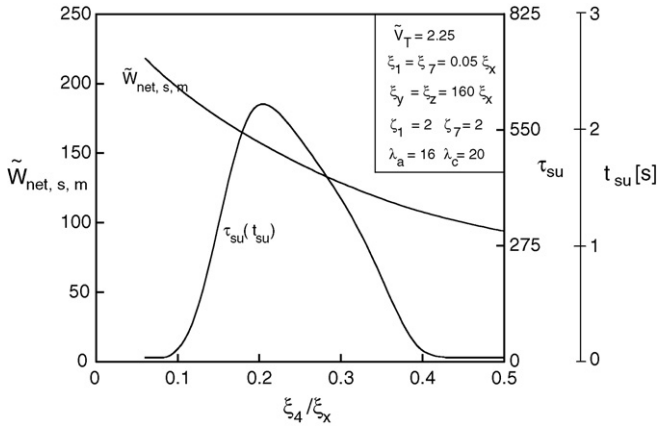

Fig. 5. The effect of membrane thickness on the one-way maximized net power.

as the membrane thickness increases, the fuel cell thermal and electrical inertias increase as well. When $\xi_4/\xi_x > 0.2$, the optimal working current decreases as the membrane thickness increases, which in turn reduces the start-up time. Fig. 5 also indicates that the membrane should be as thin as possible, down to its minimum dielectric limit, which is also restricted by the manufacturing technology. So, although Fig. 4 shows that τ_{su} increases monotonically as the reaction layers thickness increase, it also shows the one-way optimized structure leads to short start-up time for a given membrane thickness. As the membrane thickness increases, even with the one-way optimized external structure, τ_{su} increases, which is shown in Fig. 5. The useful design information is that $\xi_4/\xi_x \leq 0.08$ for short start-up time.

The previous internal structure optimization process is repeated at different external aspect ratios to produce the results shown in Fig. 6. We find that the start-up time curve departs from the values close to 0 when the external aspect ratios, ξ_y/ξ_x and ξ_z/ξ_x, are smaller than 120, and $\xi_y/\xi_x = \xi_z/\xi_x \geq 0.001$. The steady-state net power output decreases with the increment of external aspect ratios within the considered range ($\xi_y/\xi_x = \xi_z/\xi_x \geq 100$). Other external aspect ratio cases are also studied and showed in Fig. 7. The steady-state net power output reaches a maximum when the external aspect ratio is approximately 90, $\xi_y/\xi_x = \xi_z/\xi_x \geq 90$. However, the PEM fuel

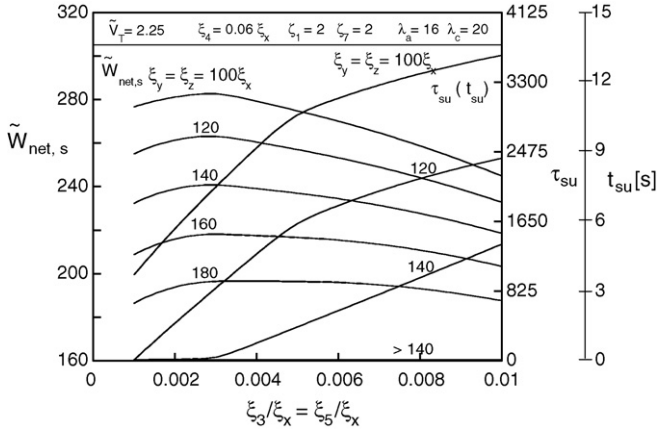

Fig. 6. The effect of external shape on net power and start-up time.

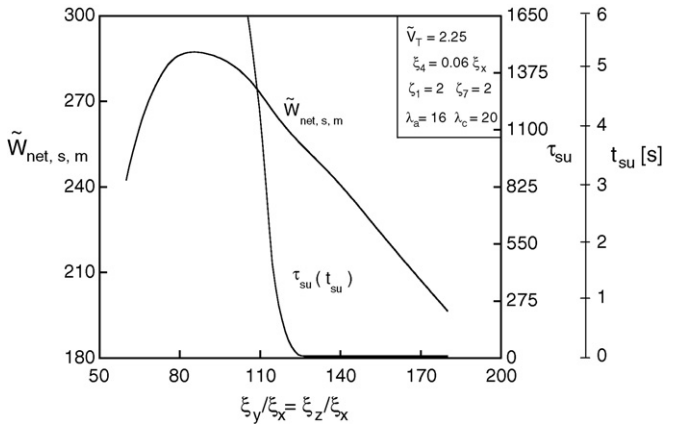

Fig. 7. The two-way net power maximization for optimal internal structure and external shape.

cell responds to the external step current loads rather slowly. The start-up time exceeds 10 s for the parameters of Table 1. In order to guarantee a short response (or start-up) time, one should increase the external aspect ratio at the expense of reducing the maximized steady-state net power output. A value of $\xi_y/\xi_x = \xi_z/\xi_x \geq 120$ leads to $\tau_{su} = 30$ (or $t_{su} \approx 0.1$ s), with a decrease of only 9% in the maximized net power output.

Several different total volumes over the range 1.0–10.0, for the stoichiometric ratios $\xi_1 = \xi_7 = 2$, are studied in Figs. 8 and 9. From Fig. 8, it is observed that there exists a critical external aspect ratio for each volume. The start-up time increases drastically when the external aspect ratio drops below those critical values. Fig. 9 shows the two-way multi-objective optima in a log–log graph, adopting the critical values for the external aspect ratio. The optimal external aspect ratios are proportional to $\tilde{V}_T^{0.2497}$, i.e., $(\xi_y/\xi_x = \xi_z/\xi_x)_{opt} = 94.3843\tilde{V}_T^{0.2497}$, and the two-way maximum steady-state net power output associated with immediate response to the external load is proportional to $\tilde{V}_T^{0.6321}$, i.e., $\tilde{W}_{net,s,mm} = 155.2745\tilde{V}_T^{0.6321}$. The effects of different stoichiometric ratios ranging from 1.0 to 10.0, on the maximum steady-state net power output and on the optimal external aspect ratio associated with the two-way multi-objective optimization along the several total

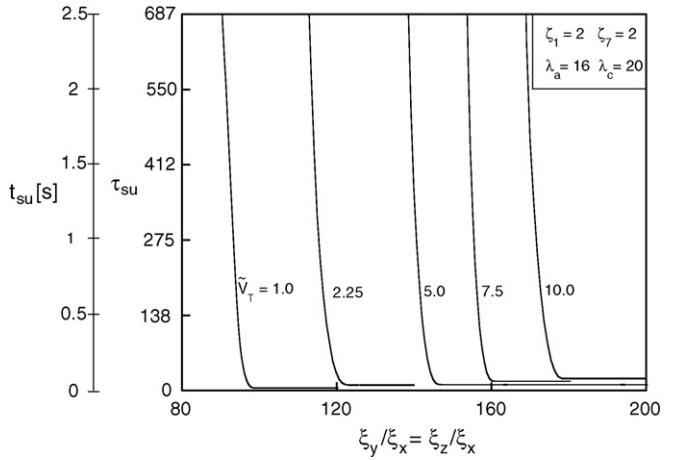

Fig. 8. The external shape effect on start-up time.

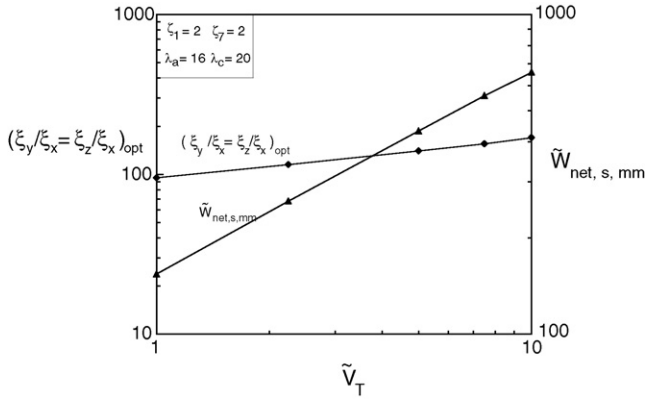

Fig. 9. The behavior of the optimal shape and the two-way maximized net power output with respect to total volume.

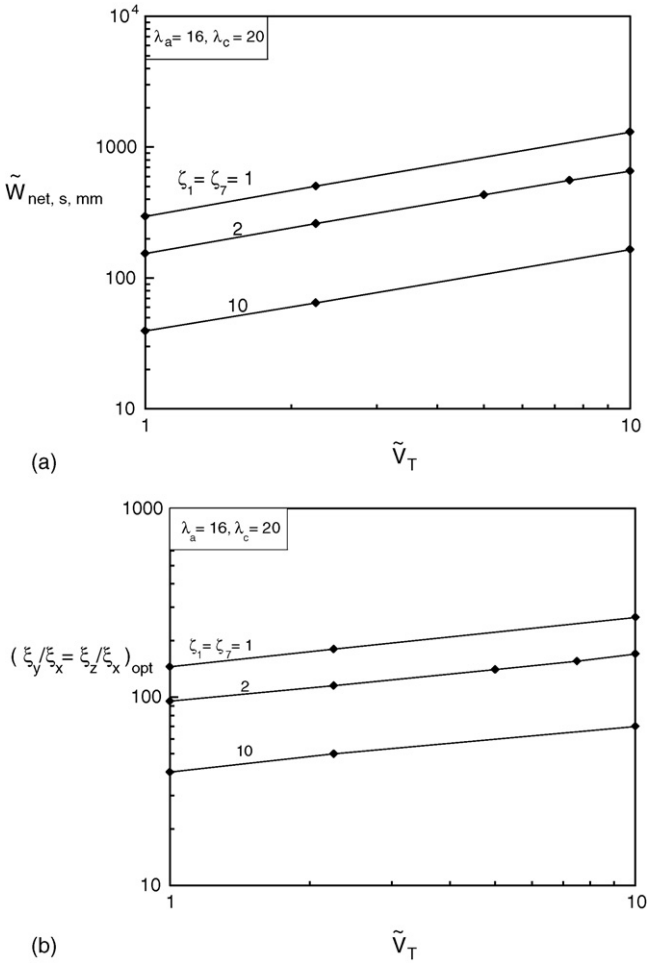

Fig. 10. The effect of stoichiometric ratio and total volume on the behavior of the two-way maximized net power (a) and optimal shape (b).

volumes over the range 1.0–10.0 are shown in Fig. 10a and b, respectively. The two-way maximized net power output fitting equations are $\tilde{W}_{net,s,mm} = 297.2350\tilde{V}_T^{0.6432}$ when $\zeta_1 = \zeta_7 = 1$, $\tilde{W}_{net,s,mm} = 155.2744\tilde{V}_T^{0.6321}$ when $\zeta_1 = \zeta_7 = 2$, and $\tilde{W}_{net,s,mm} = 39.2103\tilde{V}_T^{0.6239}$ when $\zeta_1 = \zeta_7 = 10$. The optimal aspect ratio fitting equations are $(\xi_y/\xi_x = \xi_z/\xi_x)_{opt} = 145.2446\tilde{V}_T^{0.2616}$ when $\zeta_1 = \zeta_7 = 1$,

$(\xi_y/\xi_x = \xi_z/\xi_x)_{opt} = 94.3843\tilde{V}_T^{0.2497}$ when $\zeta_1 = \zeta_7 = 2$, and $(\xi_y/\xi_x = \xi_z/\xi_x)_{opt} = 40.4390\tilde{V}_T^{0.2409}$ when $\zeta_1 = \zeta_7 = 10$. The optimal external aspect ratio is approximately proportion to $\tilde{V}_T^{1/4}$. The two-way maximized net power output is approximately proportional to $\tilde{V}_T^{0.63}$. This power–volume correlation is also found in nature. According to Randall et al. [37], the metabolic rate within a single species is around 0.63 instead of 2/3, because of the thickening of bones and other body structures in larger animals.

4. Conclusions

In this paper, we showed a multi-objective optimization of a single PEM fuel cell concentrating on vehicle applications, which require the PEM fuel cell to respond to the external load quickly and to provide as much power as possible. The internal and external shape effects on the PEM fuel cell steady state and transient response were investigated. The trade-off between the steady state net power output and the start-up time was optimally balanced in the multi-objective optimization. The geometric degrees of freedom were identified physically to be optimized, i.e., the electrodes reaction layers thickness, L_3 and L_5, and the external aspect ratios, L_y/L_x and L_z/L_x. The optima found are sharp and therefore, important to be identified in actual PEM fuel cell design.

The key conclusion is that we showed that the trade-offs exist, and that from them results the internal and external structure of a single PEM fuel cell, i.e., constructal design [20,21,22,38]. The maximum net power output is proportional to $V_T^{0.63}$. This exponent is the metabolic rate within a single species in nature. The optimal external aspect ratio is proportional to $V_T^{1/4}$. These two relations are crucial to the auxiliary power units systems (APUS) design. In principle, the multi-objective optimization illustrated in this study can be extended on a hierarchical ladder to large and more complex PEM fuel cell systems, to explore multi-scale packings that use the available volume for maximum power generation and quick response.

Acknowledgment

J.C. Ordonez, S. Chen and J.V.C. Vargas acknowledge support from NASA and ONR.

References

[1] G. Sattler, Fuel cells going on-board, J. Power Sources 86 (2000) 61–67.
[2] D. Hart, G. Hormandinger, Environmental benefits of transport and stationary fuel cells, J. Power Sources 71 (1998) 348–353.
[3] M.C. Williams, J.P. Strakey, W.A. Sudoval, The U.S. department of energy, office of fossil energy stationary fuel cells program, J. Power Sources 143 (2005) 191–196.
[4] A. Kumar, R.G. Reddy, Effect of channel dimensions and shape in the flow field distributor on the performance of polymer electrolyte membrane fuel cells, J. Power Sources 113 (2003) 11–18.
[5] J.S. Yi, T.V. Nguyen, Multicomponent transport in porous electrodes of proton exchange membrane fuel cells using the interdigitated gas distributors, J. Electrochem. Soc. 146 (1999) 38–45.
[6] T. Zhou, H. Liu, A general three-dimensional model for proton exchange membrane fuel cells, Int. J. Trans. Phenom. (2001) 177–198.
[7] M. Hu, A. Gu, M. Wang, X. Zhu, L. Yu, Three dimensional, two phase flow mathematical model for PEM fuel cell. Part I. Model development, Energy Convers. Manage. 45 (2004) 1861–1882.
[8] M. Hu, X. Zhu, M. Wang, A. Gu, L. Yu, Three dimensional, two phase flow mathematical model for PEM fuel cell. Part II. Analysis and discussion of the internal transport mechanisms, Energy Convers. Manage. 45 (2004) 1883–1916.
[9] J.C. Amphlett, R.F. Mann, B.A. Peppley, P.R. Roberge, A. Rodrigues, A model predicting transient responses of proton exchange membrane fuel cells, J. Power Sources 61 (1–2) (1996) 183–188.
[10] J. Hamelin, K. Agbossou, A. Laperriere, F. Laurencelle, T.K. Bose, Dynamic behaviour of a PEM fuel cell stack for stationary applications, Int. J. Hydrogen Energy 26 (6) (2001) 625–629.
[11] S.O. Morner, S.A. Klein, Experimental evaluation of the dynamic behavior of an air-breathing fuel cell stack, J. Solar Energy Eng.,Trans. ASME 123 (3) (2001) 225–231.
[12] H.I. Lee, C.H. Lee, T.Y. Oh, S.G. Choi, I.W. Park, K.K. Baek, Development of 1 kW class polymer electrolyte membrane fuel cell power generation system, J. Power Sources 107 (1) (2002) 110–119.
[13] T. Van Nguyen, M.W. Knobbe, A liquid water management strategy for PEM fuel cell stacks, J. Power Sources 114 (1) (2003) 70–79.
[14] M.W. Knobbe, W. He, P.Y. Chong, T.V. Nguyen, Active gas management for PEM fuel cell stacks, J. Power Sources 138 (1–2) (2004) 94–100.
[15] D. Thirumalai, R.E. White, Steady-state operation of a compressor for a proton exchange membrane fuel cell system, J. Appl. Electrochem. 30 (5) (2000) 551–559.
[16] Y.J. Zhang, M.G. Ouyang, Q.C. Lu, J.X. Luo, X.H. Li, A model predicting performance of proton exchange membrane fuel cell stack thermal systems, Appl. Thermal Eng. 24 (4) (2004) 501–513.
[17] J.J. Baschuk, X.G. Li, Modelling of polymer electrolyte membrane fuel cell stacks based on a hydraulic network approach, Int. J. Energy Res. 28 (8) (2004) 697–724.
[18] I. Mohamed, N. Jenkins, Proton exchange membrane (PEM) fuel cell stack configuration using genetic algorithms, J. Power Sources 131 (1–2) (2004) 142–146.
[19] J.V.C. Vargas, J.C. Ordonez, A. Bejan, Constructal PEM fuel cell stack design, Int. J. Heat Mass Transfer 48 (2005) 4410–4427.
[20] J.V.C. Vargas, A. Bejan, Thermodynamic optimization of internal structure in a fuel cell, Int. J. Energy Res. 28 (4) (2004) 319–339.
[21] J.V.C. Vargas, J.C. Ordonez, A. Bejan, Constructal flow structure for a PEM fuel cell, Int. J. Heat Mass Transfer 47 (2004) 4177–4193.
[22] A. Bejan, Shape and Structure from Engineering to Nature, Cambridge University Press, 2000.
[23] R.K. Shah, A.L. London, Laminar Flow Forced Convection in Ducts Supplemental to Advances in Heat Transfer, Academic Press, New York, 1978.
[24] A. Bejan, Convection Heat Transfer, 2nd ed., Wiley, New York, 1995.
[25] R.B. Bird, W.E. Stewart, E.N. Lightfoot, Transport Phenomena, 2nd ed., Wiley, New York, 2002.
[26] J.S. Newman, Electrochemical Systems, 2nd ed., Prentice Hall, Englewood Cliffs, NJ, 1991.
[27] J.A. Wesselingh, P. Vonk, G. Kraaijeveld, Exploring the Maxwell–Stefan description of ion-exchange, Chem. Eng. J. Biochem. Eng. J. 57 (1995) 75–89.
[28] M.J. Moran, R. Shapiro, Fundamentals of Engineering Thermodynamics, 3rd ed., Wiley, New York, 1993.
[29] W.L. Masterton, C.N. Hurley, Chemistry Principles and Reactions, 3rd ed., Saunders College Publishing, Orlando, FL, 1997.
[30] T.E. Springer, T.A. Zawodzinski, S. Gottesfeld, Polymer electrolyte fuel cell model, J. Electrochem. Soc. 138 (1991) 2334–2341.
[31] G. Li, P.G. Pickup, Ionic conductivity of PEMFC electrodes, J. Electrochem. Soc. 150 (2003) c745–c752.
[32] A.A. Kulikovsky, J. Divisek, A.A. Kornyshev, Two-dimensional simulation of direct methanol fuel cells—a new (embedded) type of current collector, J. Electrochem. Soc. 147 (2000) 953–959.

[33] V. Gurau, F. Barbir, H. Liu, An analytical solution of a half-cell model for PEM fuel cells, J. Electrochem. Soc. 147 (2000) 2468–2477.
[34] J.O.M. Bockris, D.M. Drazic, Electro-chemical Science, Taylor and Francis, London, 1972.
[35] A.J. Bard, L.R. Faulkner, Electrochemical Methods—Fundamentals and Applications, 2nd ed., Wiley, New York, 2001.
[36] D. Kincaid, W. Cheney, Numerical Analysis Mathematics of Scientific Computing, 1st ed., Wadsworth, Belmont, 1991.
[37] D. Randall, W. Burggren, K. French, Echert Animal Physiology: Mechanisms and Adaptations, 4th ed., W.H. Freeman, New York, 1997.
[38] A. Bejan, Constructal theory: from engineering design to predicting shape and structure in nature, Thermal Eng. 1 (1) (2001) 27–31.